Stochastic dynamical model for space-time energy spectra in turbulent shear flows

Ting Wu[1,2] and Guowei He[1,2,*]
[1]*The State Key Laboratory of Nonlinear Mechanics, Institute of Mechanics, Chinese Academy of Sciences, Beijing 100190, China*
[2]*School of Engineering Sciences, University of Chinese Academy of Sciences, Beijing 100049, China*

(Received 14 October 2020; accepted 20 April 2021; published 6 May 2021)

Space-time energy spectra describe the distribution of energy density over space and timescales, which are fundamental to studying dynamic coupling at spatial and temporal scales and turbulence-generated noise. The present paper develops a dynamic autoregressive (DAR) random forcing model for space-time energy spectra in turbulent shear flows. This model includes the two essential mechanisms of statistical decorrelation: the convection proposed by Taylor's model and the random sweeping proposed by the Kraichnan-Tennekes model. The new development is that DAR random forcing is introduced to represent the random sweeping effect. The resulting model can correctly reproduce the convection velocity and spectral bandwidths, while a white-in-time random forcing model makes erroneous predictions on spectral bandwidths. The DAR model is further combined with linear stochastic estimation (LSE) to reconstruct the near-wall velocity fluctuations of the desired space-time energy spectra. Direct numerical simulation of turbulent channel flows is used to validate the DAR model and evaluate the Werner-Wengle wall model and the LSE approach. Both the wall model and LSE incorrectly estimate the spectral bandwidths.

DOI: 10.1103/PhysRevFluids.6.054602

I. INTRODUCTION

The goal of the present paper is to develop a stochastic dynamical model for space-time energy spectra in turbulent shear flows. A space-time energy spectrum characterizes the energy distribution of velocity fluctuations over spatial and temporal lengthscales [1]. This spectrum can be used to study the spatiotemporal dynamics of turbulent flows and investigate the underlying mechanism of dominating coherent structures [2,3]. Space-time energy spectra are usually estimated from experimental measurements [4,5] and numerical simulations [6,7]. To understand the space-time energy spectrum thus obtained, we need to develop a simple stochastic model with dynamics consistent with the Navier-Stokes equations. It is our hope that the simple model not only reproduces the space-time energy spectra for theoretical studies but also provides the spatiotemporal velocity fluctuations at unresolved scales for the time-accurate large-eddy simulation of turbulence-generated noise and particle-laden turbulence.

Space-time energy spectra can be expressed by the Fourier transformation of the two-time correlations of Fourier modes of velocity fluctuations with respect to time separations. The temporal correlations of velocity modes are dominated mainly by the effects of the nonlinear terms in the Navier-Stokes equations: convection of velocity fluctuations by large-scale velocities and the self-interaction of velocity fluctuations. Large-scale convection can be represented by the

*hgw@lnm.imech.ac.cn

convection-dominating equation that originates from Taylor's hypothesis [8]. The interactions of velocity fluctuations cause energy transfers between different Fourier modes [9,10] and temporal decorrelations of Fourier modes [11]. The energy transfer can be modeled by eddy viscosity, and the temporal decorrelation can be modeled by the random sweeping hypothesis [12,13]. Therefore, a dynamic model for space-time energy spectra should include the coupling effects of large-scale convection, eddy viscosity and random sweeping.

The random sweeping hypothesis [12,13] proposes a random convection equation for space-time energy spectra in isotropic and homogeneous turbulence, which implies that the temporal decorrelation of velocity fluctuations is dominated by random convection velocities at large scales. This model is combined with Taylor's hypothesis to yield the space-time energy spectra in turbulent channel flows [7,14]. However, in the application of the random sweeping model to numerical simulation, a large sample size of random convection velocities is needed to generate an ensemble of velocity fluctuations. This incurs tremendous computational costs. An alternative is to use an external random forcing to stochastically perturb small-scale motions. In comparison with the random sweeping hypothesis, the random forcing approach is more tractable in both theoretical studies and numerical simulations. In this paper, we develop a dynamical model for the temporal correlation of Fourier modes, which uses random forcing to represent random sweeping.

The random forcing approach has been used to represent the nonlinear part of the Navier-Stokes equations for velocity fluctuations. White-in-time random forcing was introduced into the linearized Navier-Stokes equations about a mean velocity profile to investigate the energy amplification and characteristics of coherent structures [15–20]. In particular, the resolvent operator is developed to uncover elements of the coherent structures of wall turbulence [21–23]. The random forcing approach has also been used to study space-time energy spectra. Farrell and Ioannou [24] used the linearized Navier-Stokes equations with white-in-time random forcing to estimate space-time energy spectra, which characterize the coherent structures observed from experimental measurements. Zare *et al.* [25] introduced colored-in-time random forcing to replace the white-in-time random forcing in the linearized Navier-Stokes operator. The obtained results provide the temporal energy spectra at fixed wave numbers. Their model was further shown to be equivalent to the modified linearized Navier-Stokes operator with white-in-time random forcing. Morra *et al.* [26] used white-in-time and colored-in-time random forcing in a resolvent-based model for estimating space-time energy spectra in turbulent channel flows. This model with colored-in-time random forcing was found to correctly estimate the temporal energy spectra at fixed wave numbers and the cross-spectra in the wall-normal direction, especially at the characteristic length scales of buffer-layer and large-scale motions. Towne *et al.* [27] proposed determining the random forcing in the resolvent operator from the available velocity fluctuations at the outer layer and then applying the obtained random forcing to the resolvent operator at the inner layer. This method has been used to predict space-time energy spectra with several refinements [28]. The input-output analysis [29] provides a framework to investigate the space-time dynamics of fluctuations around a laminar or turbulent base flow, where input is either white-in-time or colored-in-time.

In this paper, we show that white-in-time random forcing leads to divergent bandwidths of space-time energy spectra. A space-time energy spectrum is characterized primarily by its first- and second-order moments [30]. The first-order moments conditioned at a given frequency or wave number determine the convection velocities. The second-order conditional moments determine the spectral bandwidths, which measure the well-known spectral broadening effects in turbulent flows. In fact, a divergent spectral bandwidth implies a vanishing Taylor microscale in time. To correctly reproduce the spectral bandwidths, we develop a dynamic autoregressive (DAR) forcing to represent random forcing. The DAR forcing is dependent on the previous states of both velocity fluctuations and random forcing. As a result, the dynamic models subject to the DAR forcing, which is called the DAR model in the present paper, can reproduce the space-time energy spectra with the desired convection velocities and spectral bandwidths. In the DAR model, the inputs are spatial energy spectra, convection velocity, and streamwise and spanwise sweeping velocities; the output is the space-time energy spectra. In other words, the DAR model with the known spatial energy spectra

and three constant characteristic velocities can reproduce the unknown space-time energy spectra, which have the exact first two-order conditional moments at given wave numbers. Furthermore, the DAR model yields the correct scaling of marginal distributions of space-time energy spectra such as the temporal energy spectra.

This paper is organized as follows. In Sec. II, Taylor's model with white-in-time random forcing is shown to yield divergent spectral bandwidths, where the fundamental concepts and necessary notations for space-time energy spectra used in the present paper are provided. In Sec. III, we use the Werner-Wengle (WW) wall model and the linear stochastic estimation (LSE) approach to estimate space-time energy spectra and find that both of them incorrectly estimate the spectral bandwidths. In Sec. IV, the DAR model is developed for space-time energy spectra. In Sec. V, datasets from the direct numerical simulation (DNS) of turbulent channel flows are used to verify the DAR model. In Sec. VI, conclusions and future work on the DAR model are presented.

II. TAYLOR'S MODEL WITH WHITE-IN-TIME RANDOM FORCING

We start by using the spatial Fourier modes to calculate space-time energy spectra, with the necessary notations used in the rest of the present paper, and then show that Taylor's model with white-in-time random forcing has divergent spectral bandwidths.

Consider the spatial Fourier mode of streamwise velocity fluctuations $\hat{u}(\mathbf{k}, t; y)$ at a given wall-normal location y. Here, the wave-number vector is $\mathbf{k} = (k_x, k_z)$, with k_x and k_z being the streamwise and spanwise wave numbers, respectively. In the following sections, our study focuses on a fixed wall-normal location y. For convenience, the wall-normal location y is not explicitly expressed in the physical variables. For example, $\hat{u}(\mathbf{k}, t; y)$ is simply denoted as $\hat{u}(\mathbf{k}, t)$.

A two-time correlation $\Phi(\mathbf{k}, \tau)$ of velocity Fourier mode $\hat{u}(\mathbf{k}, t)$ is defined by

$$\frac{\Phi(\mathbf{k}, \tau)}{\Phi(\mathbf{k})} = \frac{\langle \hat{u}^*(\mathbf{k}, t)\hat{u}(\mathbf{k}, t+\tau)\rangle}{\langle \hat{u}^*(\mathbf{k}, t)\hat{u}(\mathbf{k}, t)\rangle}. \tag{1}$$

Here, $\Phi(\mathbf{k})$ is the spatial energy spectrum of velocity fluctuations, and τ is the time separation. The Fourier transform of $\Phi(\mathbf{k}, \tau)$ is made with respect to τ, which yields

$$\Phi(\mathbf{k}, \omega) = \frac{1}{2\pi}\int \Phi(\mathbf{k}, \tau)e^{\mathrm{i}\omega\tau}d\tau. \tag{2}$$

Note that different independent variables are used to distinguish different energy spectra, such as $\Phi(\mathbf{k}, \omega)$ for space-time energy spectra, $\Phi(\mathbf{k})$ for spatial energy spectra and $\Phi(\omega)$ for temporal energy spectra. Similarly, $\hat{u}(\mathbf{k}, \omega)$ and $\hat{u}(\mathbf{k}, t)$ denote the space-time Fourier mode and spatial Fourier mode, respectively.

We consider Taylor's model with white-in-time random forcing

$$\frac{\partial \hat{u}(\mathbf{k}, t)}{\partial t} = -ik_x U_c \hat{u}(\mathbf{k}, t) + \hat{\sigma}(\mathbf{k}, t) \tag{3}$$

and

$$\hat{\sigma}(\mathbf{k}, t) = -c(\mathbf{k})\hat{u}(\mathbf{k}, t) + D(\mathbf{k})\hat{\xi}(\mathbf{k}, t), \tag{4}$$

where U_c is the convection velocity. In addition, $\hat{\xi}(\mathbf{k}, t)$ is a complex white-in-time random forcing: its real part $\hat{\xi}_r(\mathbf{k}, t)$ and imaginary part $\hat{\xi}_i(\mathbf{k}, t)$ are independent, which are given by

$$\langle \hat{\xi}_r(\mathbf{k}, t)\hat{\xi}_r(\mathbf{k}', t')\rangle = \langle \hat{\xi}_i(\mathbf{k}, t)\hat{\xi}_i(\mathbf{k}', t')\rangle = \delta(\mathbf{k}-\mathbf{k}')\delta(t-t'). \tag{5}$$

Noting $\hat{\xi}(\mathbf{k}, t) = \hat{\xi}_r(\mathbf{k}, t) + i\hat{\xi}_i(\mathbf{k}, t)$, we have $\langle \hat{\xi}^*(\mathbf{k}, t)\hat{\xi}(\mathbf{k}', t')\rangle = 2\delta(\mathbf{k}-\mathbf{k}')\delta(t-t')$ in which the coefficient of the variance of the random forcing $\hat{\xi}(\mathbf{k}, t)$ is 2. $D(\mathbf{k})$ is the amplitude of the random forcing, and $c(\mathbf{k})$ is a damping coefficient. In Eq. (3), the first term represents the convection effect, while the second term represents an external force. The external force consists of white-in-time

random forcing and damping forcing. The system with random forcing and damping forcing will maintain a statistically stationary state.

The solution to Eqs. (3) and (4) is

$$\hat{u}(\mathbf{k},t) = D(\mathbf{k})e^{-\mathrm{i}k_x U_c t}\int_{-\infty}^{t}\hat{\xi}(\mathbf{k},s)e^{\mathrm{i}k_x U_c s}e^{-c(\mathbf{k})(t-s)}ds, \tag{6}$$

from which we obtain

$$\langle \hat{u}^*(\mathbf{k},t)\hat{u}(\mathbf{k}',t+\tau)\rangle = \frac{D(\mathbf{k})D(\mathbf{k}')\delta(\mathbf{k}-\mathbf{k}')}{c(\mathbf{k})}e^{-c(\mathbf{k})|\tau|-\mathrm{i}k_x U_c \tau}. \tag{7}$$

The space-time energy spectra and spatial energy spectra are then found to be

$$\Phi(\mathbf{k},\omega) = \Phi(\mathbf{k})\frac{c(\mathbf{k})}{\pi[(\omega-k_x U_c)^2 + c^2(\mathbf{k})]} \tag{8}$$

and

$$\Phi(\mathbf{k}) = \int \Phi(\mathbf{k},\omega)d\omega = \frac{D^2(\mathbf{k})}{c(\mathbf{k})}. \tag{9}$$

Here, the spatial energy spectra are defined as [31]

$$\Phi(\mathbf{k})\delta(\mathbf{k}-\mathbf{k}') = \langle \hat{u}^*(\mathbf{k},t)\hat{u}(\mathbf{k}',t)\rangle. \tag{10}$$

It should be noted that the relations between the space-time energy spectra and spatial energy spectra can be found in Zare *et al.* [32].

We now calculate the first- and second-order conditional moments of the space-time energy spectra at a given wave number

$$\omega_c(\mathbf{k}) = \frac{\int \omega\Phi(\mathbf{k},\omega)d\omega}{\Phi(\mathbf{k})} = k_x U_c \tag{11}$$

and

$$B(\mathbf{k}) = \frac{\int (\omega-\omega_c)^2\Phi(\mathbf{k},\omega)d\omega}{\Phi(\mathbf{k})} = \frac{c(\mathbf{k})}{\pi}\int \frac{(\omega-k_x U_c)^2}{(\omega-k_x U_c)^2 + c^2(\mathbf{k})}d\omega = \infty. \tag{12}$$

The first expression in Eq. (11) defines the conditional mean frequencies, while the first expression in Eq. (12) defines the spectral bandwidths. The mean frequencies are often used to estimate the wave-number-dependent convection velocity, such that $c_u(\mathbf{k}) = \omega_c(\mathbf{k})/k_x$ [33]. Equation (11) shows that the white-in-time random forcing model reproduces the mean frequency, which matches the wavenumber through the convection velocity. However, the integration in the second expression of Eq. (12) is divergent.

As a result, it can be concluded from Eqs. (9) and (12) that, although the space-time energy spectra from Taylor's model with white-in-time forcing contain finite energy, their spectral bandwidths are divergent.

According to Eq. (3), we can obtain

$$\frac{\langle|\hat{\sigma}(\mathbf{k},t)|^2\rangle}{\langle|\hat{u}(\mathbf{k},t)|^2\rangle} = \frac{\langle|\partial_t\hat{u}|^2\rangle}{\langle|\hat{u}|^2\rangle} + (k_x U_c)^2 + ik_x U_c\frac{\langle\hat{u}\partial_t\hat{u}^*\rangle}{\langle|\hat{u}|^2\rangle} - ik_x U_c\frac{\langle\hat{u}^*\partial_t\hat{u}\rangle}{\langle|\hat{u}|^2\rangle}. \tag{13}$$

Using the definitions of the mean frequency and spectral bandwidth, we can find

$$\frac{\langle\hat{u}^*(\mathbf{k},t)\partial_t\hat{u}(\mathbf{k},t)\rangle}{\langle|\hat{u}(\mathbf{k},t)|^2\rangle} = -i\omega_c(\mathbf{k}) \tag{14}$$

and

$$\frac{\langle|\partial_t\hat{u}(\mathbf{k},t)|^2\rangle}{\langle|\hat{u}(\mathbf{k},t)|^2\rangle} = B(\mathbf{k}) + \omega_c^2(\mathbf{k}). \tag{15}$$

The substitution of Eqs. (14) and (15) into Eq. (13) leads to

$$\frac{\langle|\hat{\sigma}(\mathbf{k},t)|^2\rangle}{\langle|\hat{u}(\mathbf{k},t)|^2\rangle} = B(\mathbf{k}) + [\omega_c(\mathbf{k}) - k_x U_c]^2. \tag{16}$$

Therefore, in the case of $\omega_c(\mathbf{k}) = k_x U_c$, the ratio of input and output variances is the spectral bandwidth. This implies that $\langle|\hat{\sigma}(\mathbf{k},t)|^2\rangle$ is divergent if and only if $B(\mathbf{k})$ is infinite.

The Taylor microscale $\lambda_T(\mathbf{k})$ of temporal correlations of velocity modes in Eqs. (3) and (4) can be expressed in terms of the spectral bandwidths

$$\lambda_T(\mathbf{k}) = \sqrt{\frac{2\langle\hat{u}^*(\mathbf{k},t)\hat{u}(\mathbf{k},t)\rangle}{\langle\partial_t\hat{u}^*(\mathbf{k},t)\partial_t\hat{u}(\mathbf{k},t)\rangle}} = \sqrt{\frac{2}{B(\mathbf{k}) + \omega_c^2(\mathbf{k})}}. \tag{17}$$

Therefore, the divergent spectral bandwidths imply vanishing Taylor microscales. This contradicts to the nonvanishing Taylor microscales in turbulent shear flows.

III. WALL MODEL AND LSE

We use the WW wall model [34] and the spectral LSE approach [35] to estimate space-time energy spectra and compare the obtained results with the DNS results of turbulent channel flows. It is inferred that both of them incorrectly estimate the spectral bandwidths since they do not have sufficient velocity fluctuations. We present numerical evidence to confirm this inference.

A. WW wall model

We use the DNS dataset [30,36] of turbulent channel flows to evaluate the predictions of the WW wall model on space-time energy spectra: the velocities in the outer layer are used to generate the near-wall velocity fluctuations. It is then shown that the WW wall model significantly underpredicts the spectral bandwidths.

Consider the streamwise velocity component $U(x,y,z,t)$ in turbulent channel flows, where x, y, and z denote the streamwise, wall-normal, and spanwise directions, respectively. The velocity fluctuations can be calculated through

$$u(x,y,z,t) = U(x,y,z,t) - \langle U(x,y,z,t)\rangle, \tag{18}$$

where the angular bracket $\langle\rangle$ denotes the ensemble averaging which is performed in time and in the streamwise and spanwise directions due to homogeneity.

The WW wall model assumes that an instantaneous near-wall velocity profile is the piecewise combination of linear and power functions, given by

$$\frac{U(x,y,z,t)}{u_\tau(x,z,t)} = \begin{cases} \frac{yu_\tau}{\nu}, & \frac{yu_\tau}{\nu} \leqslant 11.8, \\ A\left(\frac{yu_\tau}{\nu}\right)^B, & \frac{yu_\tau}{\nu} > 11.8, \end{cases} \tag{19}$$

where $u_\tau(x,z,t)$ is the local and instantaneous friction velocity, ν is the kinematic viscosity, $A = 8.3$, and $B = 1/7$. In the present test, the velocity U_O at $y_O^+ = 92$ in the outer layer of turbulent channel flows at $\mathrm{Re}_\tau = 550$ is taken to calculate the friction velocity in terms of the second expression of Eq. (19)

$$u_\tau = \left(\frac{U_O \nu^B}{A y_O^B}\right)^{1/(B+1)}. \tag{20}$$

Here, and throughout this paper, the superscript "+" indicates normalization with wall units. The velocity U_W at $y_W^+ = 5$ in the near-wall region is then obtained according to the first expression

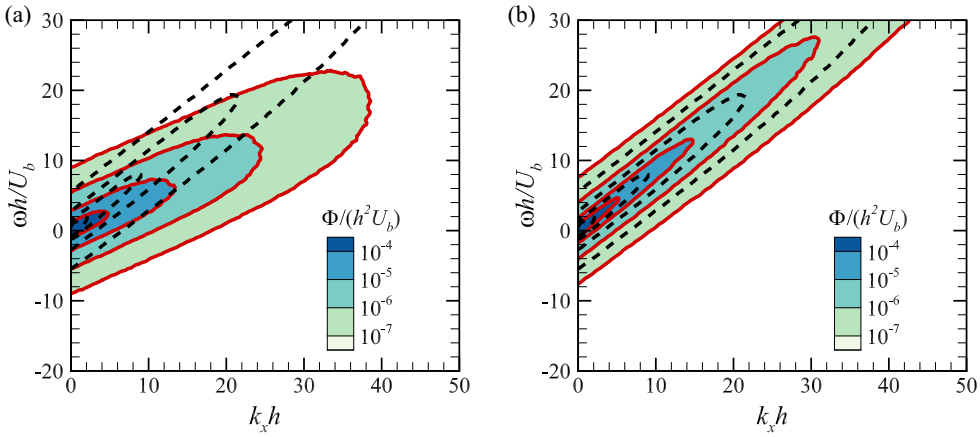

FIG. 1. Comparison of the space-time energy spectra obtained from the DNS and the WW wall model for the streamwise velocity fluctuations in turbulent channel flows at $\mathrm{Re}_\tau = 550$. (a) Contours obtained from the DNS at $y_W^+ = 5$ (colored shades with solid lines) and the WW wall model at $y_W^+ = 5$ (dashed lines). (b) Contours obtained from the DNS at $y_O^+ = 92$ (colored shades with solid lines) and the WW wall model at $y_W^+ = 5$ (dashed lines).

of Eq. (19)

$$U_W = \frac{y_W}{\nu}\left(\frac{U_O \nu^B}{A y_O^B}\right)^{2/(B+1)}. \tag{21}$$

The obtained velocity U_W is used to calculate the mean velocity, the r.m.s. of velocity fluctuations, and space-time energy spectra. The mean velocities normalized by the bulk velocity U_b, $\langle U_W \rangle / U_b$, obtained from DNS and the WW wall model are 0.26 and 0.29, respectively, which are very similar. However, the r.m.s. of velocity fluctuations $\sqrt{\langle u_W^2 \rangle}/U_b$ from the WW wall model and the DNS are 0.055 and 0.097, respectively. The first is much smaller than the second since the wall model suppresses the velocity fluctuations.

Figure 1(a) plots the isocontours of the space-time energy spectra at $y_W^+ = 5$ obtained from the WW wall model and the DNS. The preferences of isospectra from the WW wall models are more upwardly skewed than those from the DNS. The bandwidths of the cuts either in the wave number or frequency directions from the WW wall model are narrower than those from the DNS. Notably, Fig. 1(b) shows that the results from the WW wall model at $y_W^+ = 5$ are closer to the DNS results at $y_O^+ = 92$. To confirm these observations, Figs. 2(a) and 2(b) plot the convection velocities $c_u(k_x)$ and spectral bandwidths $B(k_x)$, respectively. The results from the WW wall model at $y_W^+ = 5$ are closer to the DNS results at $y_O^+ = 92$ than those at $y_W^+ = 5$. That is, the WW wall model takes the convection velocities and spectral bandwidths at the outer layers. In fact, the space-time energy spectra in the near-wall region cannot be fully determined by the flows in the outer layers, which motivates us to develop a new model for space-time energy spectra.

B. Linear stochastic estimation

Baars *et al.* [35] used the spectral LSE approach to estimate the large-scale motions in the near-wall region from the flow fields in the outer layer. In the present subsection, the velocity fields thus obtained are used to calculate the space-time energy spectra and compared with the DNS results of turbulent channel flows [30,36].

In the LSE approach, the large-scale velocities $\hat{u}^{\mathrm{L}}(\mathbf{k}, t; y_W^+)$ are estimated as follows:

$$\hat{u}^{\mathrm{L}}(\mathbf{k}, t; y_W^+) = \alpha(\mathbf{k})\hat{u}(\mathbf{k}, t; y_O^+), \tag{22}$$

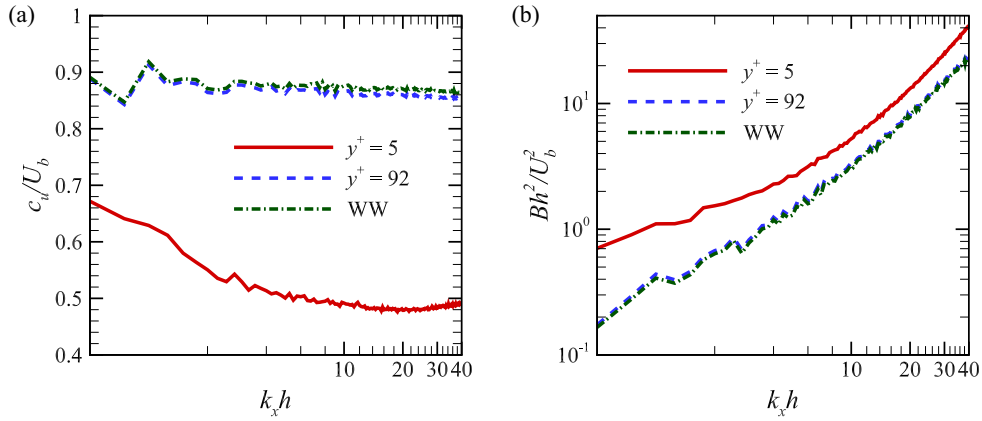

FIG. 2. (a) Wave-number-dependent convection velocities and (b) spectral bandwidths for the streamwise velocity fluctuations in turbulent channel flows at $\mathrm{Re}_\tau = 550$. The results from the DNS at $y_W^+ = 5$ are denoted by red solid lines, the results from the DNS at $y_O^+ = 92$ are denoted by blue dashed lines and the results from the WW model at $y_W^+ = 5$ are denoted by green dash-dotted lines.

where $\hat{u}(\mathbf{k}, t; y_O^+)$ denotes the velocity at location y_O^+ in the outer layer. The coefficient $\alpha(\mathbf{k})$ is determined by

$$\alpha(\mathbf{k}) = \frac{\langle \hat{u}^*(\mathbf{k}, t; y_O^+)\hat{u}(\mathbf{k}, t; y_W^+)\rangle}{\langle \hat{u}^*(\mathbf{k}, t; y_O^+)\hat{u}(\mathbf{k}, t; y_O^+)\rangle}, \tag{23}$$

where the ensemble averaging is performed in time. Consequently, we calculate the spatial energy spectra

$$\Phi^{\mathrm{L}}(\mathbf{k}; y_W^+) = |\alpha(\mathbf{k})|^2 \Phi(\mathbf{k}; y_O^+) \tag{24}$$

and the space-time energy spectra

$$\Phi^{\mathrm{L}}(\mathbf{k}, \omega; y_W^+) = |\alpha(\mathbf{k})|^2 \Phi(\mathbf{k}, \omega; y_O^+). \tag{25}$$

The velocity U_O at $y_O^+ = 92$ in the outer layer of turbulent channel flows at $\mathrm{Re}_\tau = 550$ is used to estimate the large-scale velocities $\hat{u}^{\mathrm{L}}(\mathbf{k}, t; y_W^+)$ at $y_W^+ = 5$ by the LSE method. Figure 3(a) compares the space-time energy spectra obtained from LSE and DNS. Evidently, the isocontours of the space-time energy spectra obtained are farther in the interior of those obtained from DNS. Therefore, the LSE results are significantly smaller than the DNS results. This is because the LSE results reproduce the large-scale motions but lack the small-scale motions. Figures 3(b) and 3(c) plot the convection velocities and spectral bandwidths, respectively. Similar to the result of the WW model, the convection velocities from the LSE at $y_W^+ = 5$ are closer to the DNS results at $y_O^+ = 92$ than those at $y_W^+ = 5$. In addition, the LSE also incorrectly estimates the spectral bandwidths at $y_W^+ = 5$.

IV. DAR FORCING MODEL

We will introduce DAR forcing to a simple stochastic model in the present paper, and the simple stochastic model is chosen as Taylor's model. The DAR forcing can also be introduced to the linearized Navier-Stokes operators.

A. Taylor's model with DAR forcing

The dynamic decorrelation in turbulent shear flows is mainly determined by convection, random sweeping, and distortion. The convection effects can be represented by Taylor's model, while ran-

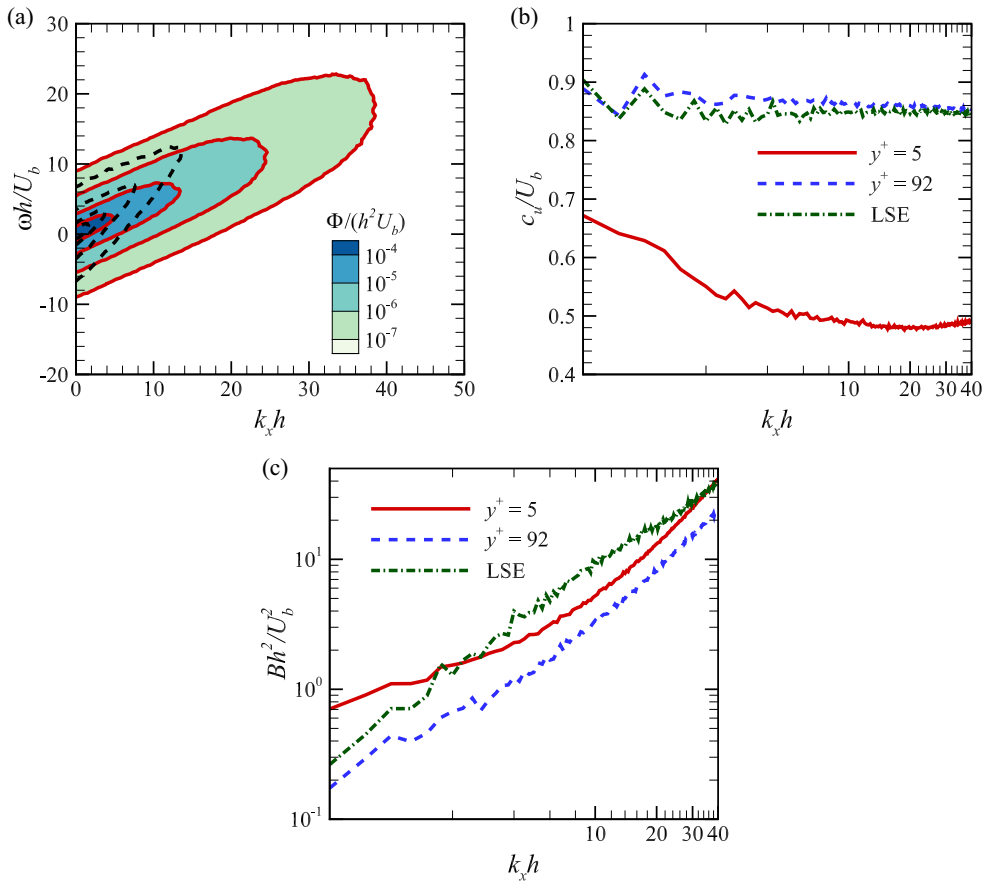

FIG. 3. Comparisons of the (a) space-time energy spectra, (b) convection velocities, and (c) spectral bandwidths obtained from the DNS and LSE for the streamwise velocity fluctuations in turbulent channel flows at $\mathrm{Re}_\tau = 550$. (a) The contours from the DNS at $y_W^+ = 5$ are denoted as colored shades with solid lines and the results from LSE at $y_W^+ = 5$ are denoted as dashed lines. (b,c) The results from the DNS at $y_W^+ = 5$ are denoted by red solid lines, the results from the DNS at $y_O^+ = 92$ are denoted by blue dashed lines and the results from the LSE at $y_W^+ = 5$ are denoted by green dash-dotted lines.

dom sweeping can be represented by the Kraichnan-Tennekes model [12,13]. In this subsection, we introduce DAR forcing to represent distortion. The linear combination of the three representations suggests the following stochastic differential equation (SDE) with random forcing:

$$\frac{\partial \hat{\upsilon}(\mathbf{k}, t)}{\partial t} = -ik_x U_c \hat{\upsilon}(\mathbf{k}, t) + \hat{\sigma}(\mathbf{k}, t), \tag{26}$$

where $\hat{\upsilon}(\mathbf{k}, t)$ is the velocity field generated in the presence of a random advection field $\mathbf{v}$ and $\mathbf{v}$ is a random sweeping velocity that satisfies a Gaussian distribution of zero mean and is constant in both space and time. The first term in the right-hand side (r.h.s.) of Eq. (26) serves as the convection with a constant convection velocity U_c. The second term in Eq. (26) consists of the three components

$$\hat{\sigma}(\mathbf{k}, t) = \hat{\sigma}_1(\mathbf{k}, t) + \hat{\sigma}_2(\mathbf{k}, t) + \hat{\sigma}_3(\mathbf{k}, t). \tag{27}$$

The three components are determined by

$$\hat{\sigma}_1(\mathbf{k}, t) = -i(\mathbf{k} \cdot \mathbf{v})\hat{\upsilon}(\mathbf{k}, t), \tag{28}$$

$$\frac{\partial \hat{\sigma}_2(\mathbf{k},t)}{\partial t} = -ik_x U_c \hat{\sigma}_2(\mathbf{k},t) - c(\mathbf{k})\hat{\sigma}_2(\mathbf{k},t) + D(\mathbf{k})\hat{\xi}(\mathbf{k},t), \tag{29}$$

$$\hat{\sigma}_3(\mathbf{k},t) = -\gamma(\mathbf{k})\hat{v}(\mathbf{k},t). \tag{30}$$

Here, $\hat{\sigma}_1(\mathbf{k},t)$ is random sweeping, $\hat{\sigma}_2(\mathbf{k},t)$ denotes external random forcing and $\hat{\sigma}_3(\mathbf{k},t)$ is the dissipation. In addition, $\gamma(\mathbf{k})$ is the dissipation coefficient; $c(\mathbf{k})$ is the damping coefficient; $\hat{\xi}(\mathbf{k},t)$ is the white-in-time random forcing given by Eq. (5), with its intensity $D(\mathbf{k})$.

The most salient feature of Eq. (29) is the external random forcing that is determined mainly by the convection and white-in-time random forcing. Dissipation and damping are introduced to maintain statistically stationary states. Equation (27) can also be considered a generalization of the previous models: it becomes Taylor's model if $\hat{\sigma}(\mathbf{k},t)$ is zero and it is the Kraichnan-Tennekes model [12,13] if U_c, $\hat{\sigma}_2(\mathbf{k},t)$, and $\hat{\sigma}_3(\mathbf{k},t)$ are zero. Wilczek and Narita's model [37] is recovered if $\hat{\sigma}_2(\mathbf{k},t)$ and $\hat{\sigma}_3(\mathbf{k},t)$ vanish.

The evolution of the first term $\hat{\sigma}_1(\mathbf{k},t)$ in Eq. (27) can be determined from Eqs. (27), (28), and (30):

$$\frac{\partial \hat{\sigma}_1(\mathbf{k},t)}{\partial t} = -ik_x U_c \hat{\sigma}_1(\mathbf{k},t) - [(\mathbf{k}\cdot\mathbf{v})^2 - i\gamma(\mathbf{k})(\mathbf{k}\cdot\mathbf{v})]\hat{v}(\mathbf{k},t) - i(\mathbf{k}\cdot\mathbf{v})\hat{\sigma}_2(\mathbf{k},t). \tag{31}$$

The evolution of the second term $\hat{\sigma}_2(\mathbf{k},t)$ in Eq. (27) can be obtained by substituting Eqs. (28) and (30) into Eq. (29):

$$\begin{aligned}\frac{\partial \hat{\sigma}_2(\mathbf{k},t)}{\partial t} &= -ik_x U_c \hat{\sigma}_2(\mathbf{k},t) - c(\mathbf{k})\hat{\sigma}(\mathbf{k},t) - ic(\mathbf{k})(\mathbf{k}\cdot\mathbf{v})\hat{v}(\mathbf{k},t) \\ &\quad - \gamma(\mathbf{k})c(\mathbf{k})\hat{v}(\mathbf{k},t) + D(\mathbf{k})\hat{\xi}(\mathbf{k},t).\end{aligned} \tag{32}$$

The evolution of the third term in Eq. (27) can be derived from Eqs. (26) and (30):

$$\frac{\partial \hat{\sigma}_3(\mathbf{k},t)}{\partial t} = -ik_x U_c \hat{\sigma}_3(\mathbf{k},t) - \gamma(\mathbf{k})\hat{\sigma}(\mathbf{k},t). \tag{33}$$

Note that in Eqs. (26), (28), (30), (31), and (32), $\hat{v}(\mathbf{k},t)$ is the velocity field generated in the presence of an advection field $\mathbf{v}$ constant in both space and time, which is not physically realistic. To generate the realistic velocity field $\hat{u}(\mathbf{k},t)$, we add Eqs. (31), (32), and (33) and then take the ensemble averaging of the resultant summation with respect to the random sweeping velocity, which gives the DAR model for the realistic velocity field $\hat{u}(\mathbf{k},t)$:

$$\frac{\partial \hat{u}(\mathbf{k},t)}{\partial t} = -ik_x U_c \hat{u}(\mathbf{k},t) + \hat{\sigma}(\mathbf{k},t), \tag{34a}$$

$$\frac{\partial \hat{\sigma}(\mathbf{k},t)}{\partial t} = -ik_x U_c \hat{\sigma}(\mathbf{k},t) - b(\mathbf{k})\hat{u}(\mathbf{k},t) - 2q(\mathbf{k})\hat{\sigma}(\mathbf{k},t) + 2\sqrt{b(\mathbf{k})q(\mathbf{k})\varphi(\mathbf{k})}\hat{\xi}(\mathbf{k},t), \tag{34b}$$

where $b(\mathbf{k}) = \langle(\mathbf{k}\cdot\mathbf{v})^2\rangle + \gamma(\mathbf{k})c(\mathbf{k})$, $q(\mathbf{k}) = [c(\mathbf{k}) + \gamma(\mathbf{k})]/2$, and $\varphi(\mathbf{k}) = D^2(\mathbf{k})/[4b(\mathbf{k})q(\mathbf{k})]$. The parameter $\varphi(\mathbf{k})$ is used to identify the amplitude of the white-in-time random forcing. The dissipation coefficient $\gamma(\mathbf{k})$ is ignorable if random sweeping is dominant over dissipation, $\langle(\mathbf{k}\cdot\mathbf{v})^2\rangle \gg \gamma(\mathbf{k})c(\mathbf{k})$, which implies

$$b(\mathbf{k}) \approx \langle(\mathbf{k}\cdot\mathbf{v})^2\rangle = k_x^2 V_x^2 + k_z^2 V_z^2. \tag{35}$$

Here, V_x is the streamwise sweeping velocity, and V_z is the spanwise sweeping velocity.

The Kraichnan-Tennekes random sweeping hypothesis implies that small-scale motions are swept by large-scale motions with little distortion [12,13]. The large-scale motions are thought to be a sweeping velocity and represented by a Gaussian random field, constant in space and time. As a result, the space-time energy spectra can be obtained over an ensemble of realizations of the Gaussian random field. In this paper, the ensemble average of the Gaussian random field is

taken, which leads to the crucial term $b(\mathbf{k})$. This makes the DAR model theoretically tractable and numerically implementable.

Equations (34a) and (34b) describe the DAR model. The time derivative of the external random forcing is determined by convection, random sweeping and white-in-time noise. As a result, the velocity modes are dependent on their past states. Therefore, the DAR model is an autoregressive process.

If $q(\mathbf{k}) = \sqrt{b(\mathbf{k})}$, the solution of the DAR model can be found as

$$\hat{u}(\mathbf{k}, t) = 2\sqrt{b^{3/2}(\mathbf{k})\varphi(\mathbf{k})}e^{-\mathrm{i}k_x U_c t}\int_{-\infty}^{t}\hat{\xi}(\mathbf{k}, s)e^{\mathrm{i}k_x U_c s}(t-s)e^{-\sqrt{b(\mathbf{k})}(t-s)}ds. \tag{36}$$

From Eq. (36), we obtain

$$\langle \hat{u}^*(\mathbf{k}, t)\hat{u}(\mathbf{k}', t+\tau)\rangle = 2\varphi(\mathbf{k})\delta(\mathbf{k}-\mathbf{k}')[1+\sqrt{b(\mathbf{k})}|\tau|]e^{-\sqrt{b(\mathbf{k})}|\tau|-\mathrm{i}k_x U_c \tau}. \tag{37}$$

Taking the time separation τ as zero in Eq. (37), we obtain the following equation for determining the parameter $\varphi(\mathbf{k})$:

$$\varphi(\mathbf{k}) = \Phi(\mathbf{k})/2. \tag{38}$$

Therefore, $\varphi(\mathbf{k})$ is proportional to the spatial energy spectrum of the desired velocity $\hat{u}(\mathbf{k}, t)$. The result in Eq. (37) directly yields the temporal correlations of velocity modes

$$\Phi(\mathbf{k}, \tau) = \Phi(\mathbf{k})(1+\sqrt{b(\mathbf{k})}|\tau|)e^{-\sqrt{b(\mathbf{k})}|\tau|-\mathrm{i}k_x U_c \tau} \tag{39}$$

and the space-time energy spectra

$$\Phi(\mathbf{k}, \omega) = \Phi(\mathbf{k})\frac{2b^{3/2}(\mathbf{k})}{\pi[(\omega-k_x U_c)^2+b(\mathbf{k})]^2}. \tag{40}$$

There are two other solutions to the DAR model. If $q(\mathbf{k}) < \sqrt{b(\mathbf{k})}$, we find the temporal correlations of velocity modes

$$\Phi(\mathbf{k}, \tau) = \Phi(\mathbf{k})\frac{q\sin(\sqrt{b-q^2}|\tau|)+\sqrt{b-q^2}\cos(\sqrt{b-q^2}|\tau|)}{\sqrt{b-q^2}}e^{-q|\tau|-\mathrm{i}k_x U_c \tau}. \tag{41}$$

If $q(\mathbf{k}) > \sqrt{b(\mathbf{k})}$, we find the temporal correlations of velocity modes

$$\Phi(\mathbf{k}, \tau) = \frac{\Phi(\mathbf{k})}{2\sqrt{q^2-b}}[(q+\sqrt{q^2-b})e^{-(q-\sqrt{q^2-b})|\tau|}-(q-\sqrt{q^2-b})e^{-(q+\sqrt{q^2-b})|\tau|}]e^{-\mathrm{i}k_x U_c \tau}. \tag{42}$$

The temporal correlation in Eq. (41) with $U_c = 0$ does not decay monotonically but oscillates, which is inconsistent with the monotonic Gaussian decay predicted by the random sweeping model. The correlation in Eq. (42) with $U_c = 0$ is the bi-exponential form, which decays too slowly compared with Gaussian decay. Therefore, $q(\mathbf{k}) = \sqrt{b(\mathbf{k})}$ and the corresponding temporal correlation in Eq. (39) are taken to be consistent with the random sweeping model.

Equation (39) implies the exponential decay of the temporal correlations, especially for large time separations, while the algebraic factor modifies the small separations. Equation (40) shows that the convection velocity characterizes the Doppler shift effect and, most importantly, that random sweeping characterizes the Doppler broadening effect [7]. This can be further confirmed from the conditional mean frequencies and bandwidths of space-time energy spectra, given by

$$\omega_c(\mathbf{k}) = \frac{\int \omega\Phi(\mathbf{k}, \omega)d\omega}{\Phi(\mathbf{k})} = k_x U_c \tag{43}$$

and

$$B(\mathbf{k}) = \frac{\int (\omega - \omega_c)^2 \Phi(\mathbf{k}, \omega) d\omega}{\Phi(\mathbf{k})} = b(\mathbf{k}). \tag{44}$$

Therefore, the DAR model exactly reproduces the mean frequencies and spectral bandwidths.

The DAR model can also produce the same scaling of the temporal energy spectra as Kolmogorov's theory. If Kolmogorov scaling is taken for spatial energy spectra, such as $\Phi(k_x) \propto |k_x|^{-5/3}$, and $b(\mathbf{k})$ is approximately taken as $k_x^2 V_x^2$, then

$$\begin{aligned}\Phi(\omega) = \int \Phi(\mathbf{k}, \omega) d\mathbf{k} &\sim \int \Phi(k_x) \frac{|k_x|^3}{\left[(\omega - k_x U_c)^2 + k_x^2 V_x^2\right]^2} dk_x \\ &\sim |\omega|^{-5/3} \int \frac{|\beta|^{4/3}}{\left[(1 - \beta U_c)^2 + \beta^2 V_x^2\right]^2} d\beta \sim |\omega|^{-5/3},\end{aligned} \tag{45}$$

where the transformation of the integral variable, $\beta = k_x/\omega$, is used in the third expression of Eq. (45).

It is illuminating to compare the DAR forcing with the white-in-time and colored-in-time random forcing as follows.

(i) The first term $\hat{\sigma}_1(\mathbf{k}, t)$ in the DAR forcing represents the random sweeping effect in turbulent flows. The white-in-time forcing excludes the random sweeping effect.

(ii) The second term $\hat{\sigma}_2(\mathbf{k}, t)$ in the DAR forcing is the filtered white-in-time random forcing, which is similar to the filter parametrization proposed by Zare *et al.* [25].

(iii) In the DAR model, no white-in-time random forcing is directly imposed on the velocity component $\hat{u}(\mathbf{k}, t)$. It is shown that white-in-time random forcing leads to divergent spectral bandwidths.

In the DAR model, Taylor's model is used to account for convection. As a result, the linear part of the DAR model is the simplest form of the linearized NS equations. The derivative of the external forcing is governed by random sweeping, damping, and white-in-time noise. Therefore, the governing equations for the state variable (streamwise velocities) are second-order autoregressive processes. It is noted that the state variables in the present paper are not directly dependent on white-in-time noise, which avoids divergent spectral bandwidths. It is shown that the colored-in-time noise proposed by Zare *et al.* [25] for the linearized NS equations is equivalent to the modified linearized NS equations with white-in-time noise. However, input-output analysis has the flexibility for different external forces and provides a general and useful framework to study wall-bounded turbulence [29].

Zare *et al.* [25], Morra *et al.* [26], and Towne *et al.* [27] used the linearized NS equations to predict two-point velocity correlations in the wall-normal direction. This implies that if the DAR forcing is applied to the linearized NS equations and the resolvent operator, it is possible that the DAR model may reproduce not only the space-time velocity fields and space-time energy spectra at different wall-normal positions, but also the space-time two-point velocity correlations in the wall-normal direction. However, the present paper is limited to Taylor's model.

B. Determination of the parameters in the DAR model

The propagation velocity and bandwidths of temporal spectra conditioned at fixed wave numbers are used to determine the following parameters in the DAR model: convection velocity U_c, streamwise sweeping velocity V_x, and spanwise sweeping velocity V_z.

The convection velocity can be determined by space-time correlations

$$U_c = -\left.\frac{\partial^2_{r\tau} R(r, \tau)}{\partial^2_{rr} R(r, \tau)}\right|_{r=0\ \ \tau=0}, \tag{46}$$

where the space-time correlations are defined as

$$R(r,\tau) = \langle u(x,y,z,t)u(x+r,y,z,t+\tau)\rangle = \iint \Phi(k_x,\omega)e^{\mathrm{i}(k_x r-\omega\tau)}dk_x d\omega. \tag{47}$$

Here, $R(r,\tau)$ denotes the space-time correlation of streamwise velocity fluctuations at the wall-normal location y, $\Phi(k_x,\omega)$ denotes the corresponding space-time energy spectra and $\langle\rangle$ denotes the ensemble averaging with respect to the streamwise coordinate x, spanwise coordinate z, and time t. However, the dependence of the energy spectra and correlation function on the wall-normal coordinate y is not explicitly indicated in the present subsection.

The substitution of Eq. (47) into Eq. (46) gives

$$U_c = \frac{\int c_u(k_x)k_x^2\Phi(k_x)dk_x}{\int k_x^2\Phi(k_x)dk_x}, \tag{48}$$

where

$$c_u(k_x) = \frac{\omega_c(k_x)}{k_x}, \tag{49}$$

and

$$\omega_c(k_x) = \frac{\int \omega\Phi(k_x,\omega)d\omega}{\Phi(k_x)}. \tag{50}$$

In this case, $c_u(k_x)$ is the convection velocity of Fourier mode $\hat{u}(k_x,t;y)$, and $\omega_c(k_x)$ is the mean frequency of space-time energy spectra $\Phi(k_x,\omega)$ at a given wave number k_x. Equation (48) is the same as the definition given by Del Álamo and Jiménez [33].

We now calculate the bandwidths of the frequency spectra for a fixed wave number k_x

$$\begin{aligned} B(k_x) &= \frac{\int [\omega-\omega_c(k_x)]^2\Phi(k_x,\omega)d\omega}{\Phi(k_x)} \\ &= \frac{\int (\omega-k_xU_c)^2\Phi(k_x,\omega)d\omega}{\Phi(k_x)} \\ &= \frac{\iint (\omega-k_xU_c)^2\Phi(k_x,k_z,\omega)dk_z d\omega}{\Phi(k_x)} \\ &= k_x^2V_x^2 + V_z^2\frac{\int k_z^2\Phi(k_x,k_z)dk_z}{\int \Phi(k_x,k_z)dk_z}. \end{aligned} \tag{51}$$

In the above derivation, the mean frequency in the first equation is replaced by Eq. (50); the space-time energy spectra $\Phi(k_x,\omega)$ in the second equation are replaced by $\int \Phi(k_x,k_z,\omega)dk_z$; and the space-time energy spectra in the third equation are replaced by the DAR model. Taking the wave number k_x as zero in Eq. (51), we obtain the following equation for determining the spanwise sweeping velocity V_z:

$$V_z^2 = \left.\frac{B(k_x)\int \Phi(k_x,k_z)dk_z}{\int k_z^2\Phi(k_x,k_z)dk_z}\right|_{k_x=0}. \tag{52}$$

We further calculate the weighted average of spectral bandwidths

$$\frac{\int B(k_x)\Phi(k_x)dk_x}{\int k_x^2\Phi(k_x)dk_x} = V_x^2 + V_z^2\frac{\int k_z^2\Phi(k_z)dk_z}{\int k_x^2\Phi(k_x)dk_x}, \tag{53}$$

in which the spectral bandwidth $B(k_x)$ is replaced by Eq. (51). Equation (53) is used to determine the streamwise sweeping velocity V_x

$$V_x^2 = \frac{\int B(k_x)\Phi(k_x)dk_x}{\int k_x^2\Phi(k_x)dk_x} - V_z^2\frac{\int k_z^2\Phi(k_z)dk_z}{\int k_x^2\Phi(k_x)dk_x}. \tag{54}$$

The random sweeping velocity in the elliptic approximation (EA) model [38,39] for space-time correlations can be expressed as

$$V_{\mathrm{EA}}^2 = \frac{\int B(k_x)\Phi(k_x)dk_x}{\int k_x^2\Phi(k_x)dk_x} + \left\{\frac{\int c_u^2(k_x)k_x^2\Phi(k_x)dk_x}{\int k_x^2\Phi(k_x)dk_x} - \left[\frac{\int c_u(k_x)k_x^2\Phi(k_x)dk_x}{\int k_x^2\Phi(k_x)dk_x}\right]^2\right\}. \tag{55}$$

The first term in the r.h.s. of Eq. (55) represents the contribution of the spectral bandwidths to the random sweeping velocity in the EA model. The second term represents the contribution of the different velocity modes to the random sweeping velocity in the EA model, which becomes zero if the convection velocities of different velocity modes are independent of wave numbers. Therefore, Eq. (55) justifies that Eq. (53) is reasonable to determine the random sweeping velocity.

C. Reconstruction of near-wall velocity fields and energy spectra

The DAR model in combination with LSE can be used to generate the near-wall velocity fields using the outer-layer velocity fields in turbulent channel flows. The DAR model generates velocity fluctuations in the near-wall region, while LSE provides large-scale velocities in the same regions. Their linear combination can produce near-wall velocities with the correct spectral bandwidths.

The near-wall velocity fields are assumed to be the sum of two parts, given by

$$\hat{u}(\mathbf{k}, t; y_W) = \hat{u}^{\mathrm{L}}(\mathbf{k}, t; y_W) + \hat{u}^{\mathrm{R}}(\mathbf{k}, t; y_W), \tag{56}$$

where the LSE part $\hat{u}^{\mathrm{L}}(\mathbf{k}, t; y_W)$ represents the large-scale part and the remaining part $\hat{u}^{\mathrm{R}}(\mathbf{k}, t; y_W)$ is generated from the DAR model. The LSE part $\hat{u}^{\mathrm{L}}$ and the remaining part $\hat{u}^{\mathrm{R}}$ are independent since $\hat{u}^{\mathrm{R}}$ is generated from $\hat{\xi}$. $\hat{\xi}$ is independently generated in the simulation and thus independent of $\hat{u}^{\mathrm{L}}$ even for different time. Thus, we have

$$\langle \hat{u}^{\mathrm{L}*}(\mathbf{k}, t; y_W)\hat{u}^{\mathrm{R}}(\mathbf{k}, t; y_W)\rangle = \langle \hat{u}^{\mathrm{L}*}(\mathbf{k}, t; y_W)\rangle\langle \hat{u}^{\mathrm{R}}(\mathbf{k}, t; y_W)\rangle = 0 \tag{57}$$

and

$$\langle \hat{u}^{\mathrm{L}*}(\mathbf{k}, \omega; y_W)\hat{u}^{\mathrm{R}}(\mathbf{k}, \omega; y_W)\rangle = \langle \hat{u}^{\mathrm{L}*}(\mathbf{k}, \omega; y_W)\rangle\langle \hat{u}^{\mathrm{R}}(\mathbf{k}, \omega; y_W)\rangle = 0. \tag{58}$$

Therefore, the spatial energy spectra and the space-time energy spectra obtained from the DAR model in combination with LSE are given by

$$\Phi(\mathbf{k}; y_W) = \Phi^{\mathrm{L}}(\mathbf{k}; y_W) + \Phi^{\mathrm{R}}(\mathbf{k}; y_W) \tag{59}$$

and

$$\Phi(\mathbf{k}, \omega; y_W) = \Phi^{\mathrm{L}}(\mathbf{k}, \omega; y_W) + \Phi^{\mathrm{R}}(\mathbf{k}, \omega; y_W), \tag{60}$$

where Φ^{L} denotes the energy spectra obtained from LSE and Φ^{R} denotes those from the DAR model.

The detailed procedure for estimating the near-wall velocity fields is described as follows.

(i) LSE is used to estimate the large-scale velocities $\hat{u}^{\mathrm{L}}(\mathbf{k}, t; y_W)$ at the near-wall location y_W from the outer-layer velocities $\hat{u}(\mathbf{k}, t; y_O)$ at the location y_O

$$\hat{u}^{\mathrm{L}}(\mathbf{k}, t; y_W) = \alpha(\mathbf{k})\hat{u}(\mathbf{k}, t; y_O), \tag{61}$$

and

$$\alpha(\mathbf{k}) = \frac{\langle \hat{u}^*(\mathbf{k}, t; y_O)\hat{u}(\mathbf{k}, t; y_W)\rangle}{\langle \hat{u}^*(\mathbf{k}, t; y_O)\hat{u}(\mathbf{k}, t; y_O)\rangle}. \tag{62}$$

Then, the spatial energy spectra $\Phi^{\mathrm{L}}(\mathbf{k}; y_W)$ and the space-time energy spectra $\Phi^{\mathrm{L}}(\mathbf{k}, \omega; y_W)$ of the large-scale part can be obtained by Eqs. (24) and (25).

(ii) The DAR model is used to generate the remaining part $\hat{u}^{\mathrm{R}}(\mathbf{k}, t; y_W)$ of the near-wall velocity fluctuations, where the parameters $\varphi(\mathbf{k})$, U_c, V_x, and V_z are determined from the energy spectra, $\Phi^{\mathrm{R}}(\mathbf{k}; y_W)$ and $\Phi^{\mathrm{R}}(\mathbf{k}, \omega; y_W)$, of the remaining part by using Eq. (38) and the method in Sec. IV B. The remaining energy spectra $\Phi^{\mathrm{R}}(\mathbf{k}; y_W)$ and $\Phi^{\mathrm{R}}(\mathbf{k}, \omega; y_W)$ are calculated from

$$\Phi^{\mathrm{R}}(\mathbf{k}; y_W) = \Phi(\mathbf{k}; y_W) - \Phi^{\mathrm{L}}(\mathbf{k}; y_W), \tag{63}$$

$$\Phi^{\mathrm{R}}(\mathbf{k}, \omega; y_W) = \Phi(\mathbf{k}, \omega; y_W) - \Phi^{\mathrm{L}}(\mathbf{k}, \omega; y_W). \tag{64}$$

It should be emphasized that because the DAR model is performed to generate only the remaining part of the near-wall velocity fields, it is necessary to use the remaining energy spectra $\Phi^{\mathrm{R}}(\mathbf{k}; y_W)$ and $\Phi^{\mathrm{R}}(\mathbf{k}, \omega; y_W)$ to estimate the parameters. It is noted that the superscript "R" is omitted for brevity in Eq. (38) and Sec. IV B.

(iii) The near-wall velocities are the sum of these two parts, as indicated in Eq. (56), and the velocity fields can be obtained by the Fourier transform of $\hat{u}(\mathbf{k}, t; y_W)$

$$u(x, z, t; y_W) = \iint \hat{u}(\mathbf{k}, t; y_W) e^{\mathrm{i}(k_x x + k_z z)} dk_x dk_z. \tag{65}$$

Consequently, the space-time energy spectra are given by Eq. (60), and the temporal correlations of the Fourier modes are given by

$$\Phi(\mathbf{k}, \tau; y_W) = \Phi^{\mathrm{L}}(\mathbf{k}, \tau; y_W) + \Phi^{\mathrm{R}}(\mathbf{k}, \tau; y_W). \tag{66}$$

Then, $\Phi(k_x, \omega; y_W)$ and $\Phi(k_x, \tau; y_W)$ can be obtained by integrating $\Phi(\mathbf{k}, \omega; y_W)$ and $\Phi(\mathbf{k}, \tau; y_W)$, respectively, with respect to the spanwise wave number k_z:

$$\Phi(k_x, \omega; y_W) = \int \Phi(\mathbf{k}, \omega; y_W) dk_z, \tag{67}$$

$$\Phi(k_x, \tau; y_W) = \int \Phi(\mathbf{k}, \tau; y_W) dk_z. \tag{68}$$

Finally, the space-time correlation can be obtained by the Fourier transform of $\Phi(k_x, \tau; y_W)$:

$$R(r, \tau; y_W) = \int \Phi(k_x, \tau; y_W) e^{\mathrm{i}k_x r} dk_x. \tag{69}$$

V. NUMERICAL RESULTS

Two DNS datasets of the turbulent channel flows at $\mathrm{Re}_\tau \equiv u_\tau h/\nu = 550$ and $\mathrm{Re}_\tau = 180$ are used to validate the DAR model, where u_τ is the friction velocity, h is the channel half-height and ν is the kinematic viscosity. A pseudospectral method with a 3/2 de-aliasing rule is performed to numerically solve the Navier-Stokes equations. Periodic boundary conditions are used in the streamwise and spanwise directions, and no-slip boundary conditions are applied at the walls. For the DNS at $\mathrm{Re}_\tau = 550$, the computational domain is $8\pi h \times 2h \times 3\pi h$ in the streamwise (x), wall-normal (y), and spanwise (z) directions, respectively, in which there are $1536 \times 256 \times 1152$ grid points. The time step is taken as $\Delta t = 1.25 \times 10^{-3} h/U_b$ ($\Delta t^+ \approx 0.037$), where U_b is the bulk velocity. The instantaneous flow fields are stored every eight steps during a period of $20.48h/U_b$ in the statistically stationary state. For the DNS at $\mathrm{Re}_\tau = 180$, the computational domain is $2\pi h \times 2h \times \pi h$ in the streamwise, wall-normal, and spanwise directions, respectively, in which there are $128 \times 128 \times 128$ grid points. The time step is taken as $\Delta t = 1 \times 10^{-3} h/U_b$ ($\Delta t^+ \approx 0.011$). The instantaneous flow fields are stored every ten steps during a period of $163.84h/U_b$ in the statistically stationary state. The Navier-Stokes solver and the dataset have been validated and used in previous studies [30,36,40].

TABLE I. Parameters in the DAR model. The convection velocity U_c is normalized by the bulk velocity U_b, and the streamwise sweeping velocity V_x and spanwise sweeping velocity V_z are normalized by the friction velocity u_τ.

Case	U_c/U_b	V_x/u_τ	V_z/u_τ
$y^+ = 270$ ($\mathrm{Re}_\tau = 550$)	1.02	1.43	0.924
$y^+ = 5$ ($\mathrm{Re}_\tau = 550$)	0.484	2.84	0.599
$y^+ = 5$ ($\mathrm{Re}_\tau = 180$)	0.612	2.42	0.598

The spatial Fourier mode is calculated by

$$\hat{u}(k_x, t; y, z) = \frac{1}{L_x}\int_0^{L_x} u(x, t; y, z)\exp(-ik_x x)dx, \tag{70}$$

where L_x is the domain size in the streamwise direction. The space-time Fourier mode is calculated by

$$\tilde{u}(k_x, \omega; y, z) = \frac{1}{\sqrt{T\int_0^T w(t)^2 dt}}\int_0^T w(t)\hat{u}(k_x, t; y, z)e^{i\omega t}dt. \tag{71}$$

Here, $w(t)$ is the Hanning window, and T is the temporal interval length taken as $T = 20.48h/U_b$ at $\mathrm{Re}_\tau = 550$ and $T = 10.24h/U_b$ at $\mathrm{Re}_\tau = 180$. The space-time energy spectrum is calculated by

$$\Phi(k_x, \omega; y) = \frac{\langle \tilde{u}^*(k_x, \omega; y, z)\tilde{u}(k_x, \omega; y, z)\rangle}{\Delta k_x \Delta\omega}, \tag{72}$$

where $\Delta k_x = 2\pi/L_x$, $\Delta\omega = 2\pi/T$, and the ensemble average is performed in time and in the spanwise direction.

The DAR model without LSE is applied at $y^+ = 270$ in the outer layer at $\mathrm{Re}_\tau = 550$. In this case, the parameters in the DAR model are taken as shown in the first line of Table I. Figure 4 compares the contours of the space-time energy spectra and the temporal spectra for three different

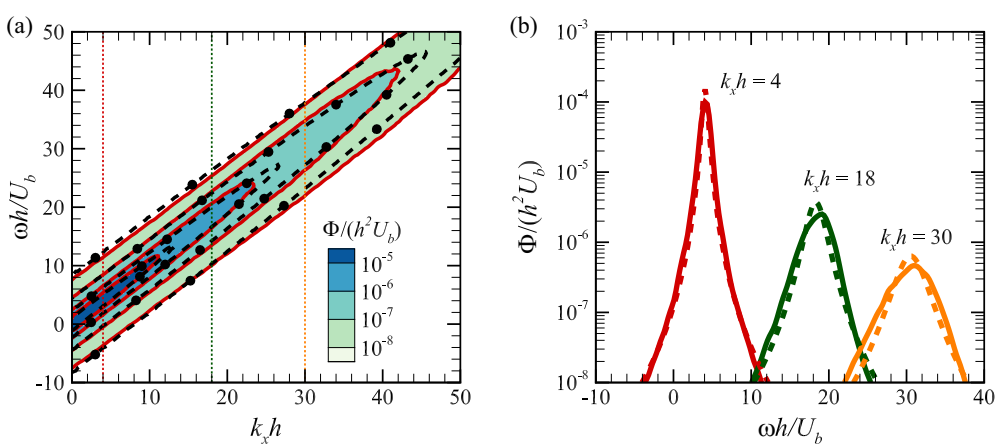

FIG. 4. Comparison of the space-time energy spectra obtained from the DNS and the DAR model for the streamwise velocity fluctuations at $y^+ = 270$ in turbulent channel flows at $\mathrm{Re}_\tau = 550$. (a) Contours obtained from the DNS (colored shades with solid lines) and the DAR model (dashed lines with dots). (b) Cuts through space-time energy spectra at three different wave numbers obtained from the DNS (colored solid lines) and the DAR model (dashed lines).

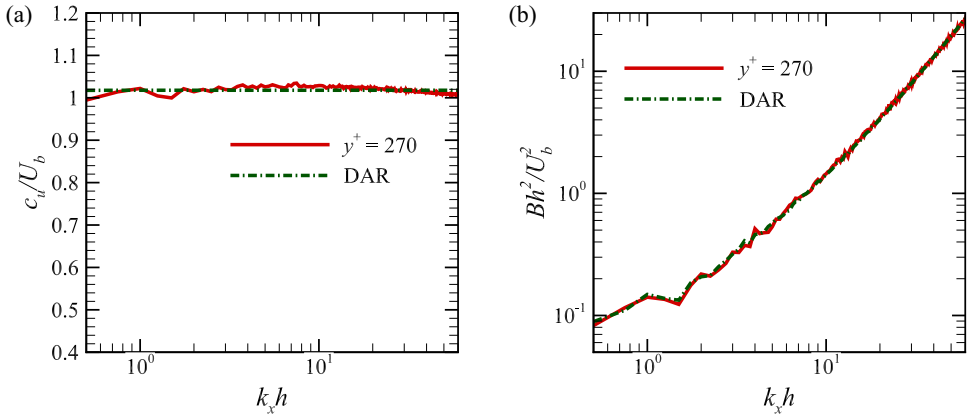

FIG. 5. (a) Wave-number-dependent convection velocities and (b) spectral bandwidths for the streamwise velocity fluctuations at $y^+ = 270$ in turbulent channel flows at $\mathrm{Re}_\tau = 550$. The results from the DNS are denoted by red solid lines, and the results from the DAR model are denoted by green dash-dotted lines.

wave numbers from the DAR model and the DNS. Figure 5 compares the wave-number-dependent convection velocities and spectral bandwidths obtained from the DAR model and the DNS. Figure 6 plots the line and shade contours of the space-time correlations and the spatial correlations for fixed delay times. All the results in Figs. 4, 5, and 6 from the present model are in agreement with those of DNS, indicating that the DAR model alone can correctly reproduce the space-time energy spectra of velocity fluctuations in the outer layer.

To correctly characterize the space-time energy spectra in the inner layer, especially the wave-number-dependent convection velocities, LSE should be used to determine the large-scale motions. For the case of $y_W^+ = 5$ at $\mathrm{Re}_\tau = 550$, the velocities at $y_O^+ = 92$ are used to perform the LSE. For the case of $y_W^+ = 5$ at $\mathrm{Re}_\tau = 180$, the velocities at $y_O^+ = 80$ are used to perform the LSE. The parameters in the DAR model for the two cases are shown in Table I. In addition to these outer-layer locations,

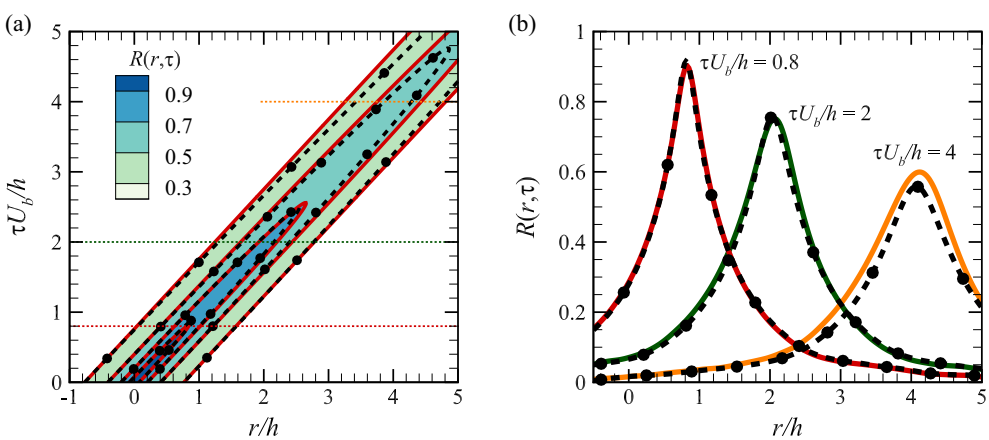

FIG. 6. Comparison of the space-time correlations obtained from the DNS and the DAR model for streamwise velocity fluctuations at $y^+ = 270$ in turbulent channel flows at $\mathrm{Re}_\tau = 550$. (a) Contours obtained from the DNS (colored shades with solid lines) and the DAR model (dashed lines with dots). (b) Cuts through space-time correlations at three different temporal separations obtained from the DNS (colored solid lines) and the DAR model (dashed lines with dots).

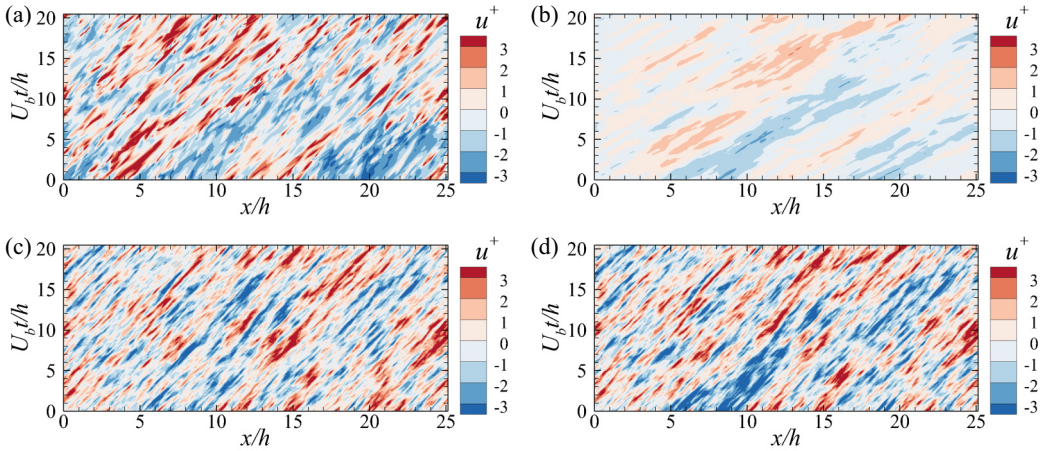

FIG. 7. Temporal evolutions of the streamwise velocity fluctuations at $y_W^+ = 5$ in turbulent channel flows at $\mathrm{Re}_\tau = 550$. (a) The DNS results. (b) The LSE results. (c) The results from the DAR model. (d) The results from the DAR model with LSE.

we also take $y_O^+ = 44$ and $y_O^+ = 270$ for $\mathrm{Re}_\tau = 550$ and $y_O^+ = 46$ and $y_O^+ = 180$ for $\mathrm{Re}_\tau = 180$ as the outer-layer locations. When different outer-layer locations are taken, the parameters in the DAR model are only slightly changed, and the results obtained, including the space-time energy spectra, wave-number-dependent convection velocities and spectral bandwidths, are very similar and not shown in this paper.

Figure 7 plots the temporal evolutions of the spatial distributions of the streamwise velocity components at $y_W^+ = 5$ obtained by the DNS, LSE, DAR model and the combination of the DAR model with LSE. The LSE results lack velocity fluctuations, and the preference angles of the velocity contours obtained from LSE are significantly smaller than those from the DNS. Noting that the horizontal axis represents the spatial direction and the vertical axis represents time, this observation is consistent with the result that the convection velocities obtained by LSE are larger than those of DNS. The DAR results look similar to the DNS results but exhibit fewer large-scale structures. The velocity contours obtained from the combined DAR and LSE model are in good agreement with those from the DNS. In particular, the preference directions of velocity contours in the DAR

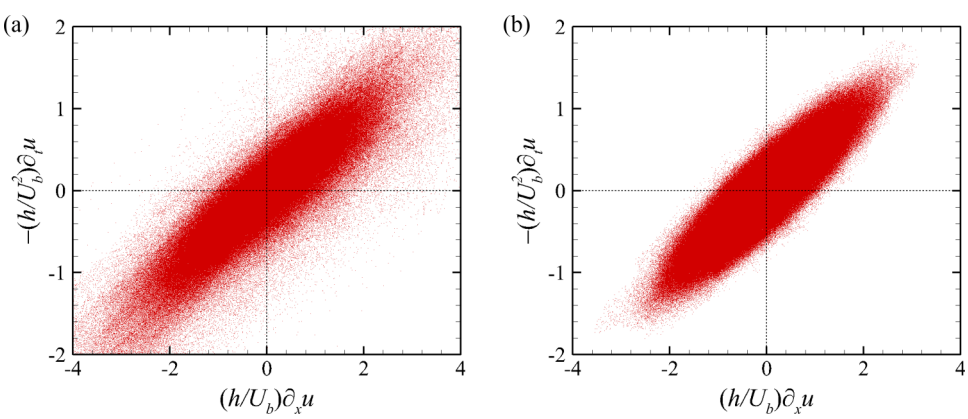

FIG. 8. Scatter plot of the normalized temporal derivatives $-(h/U_b^2)\partial_t u$ vs. the normalized spatial derivatives $(h/U_b)\partial_x u$ for $y_W^+ = 5$ at $\mathrm{Re}_\tau = 550$. (a) The DNS result. (b) The result from the DAR model with LSE.

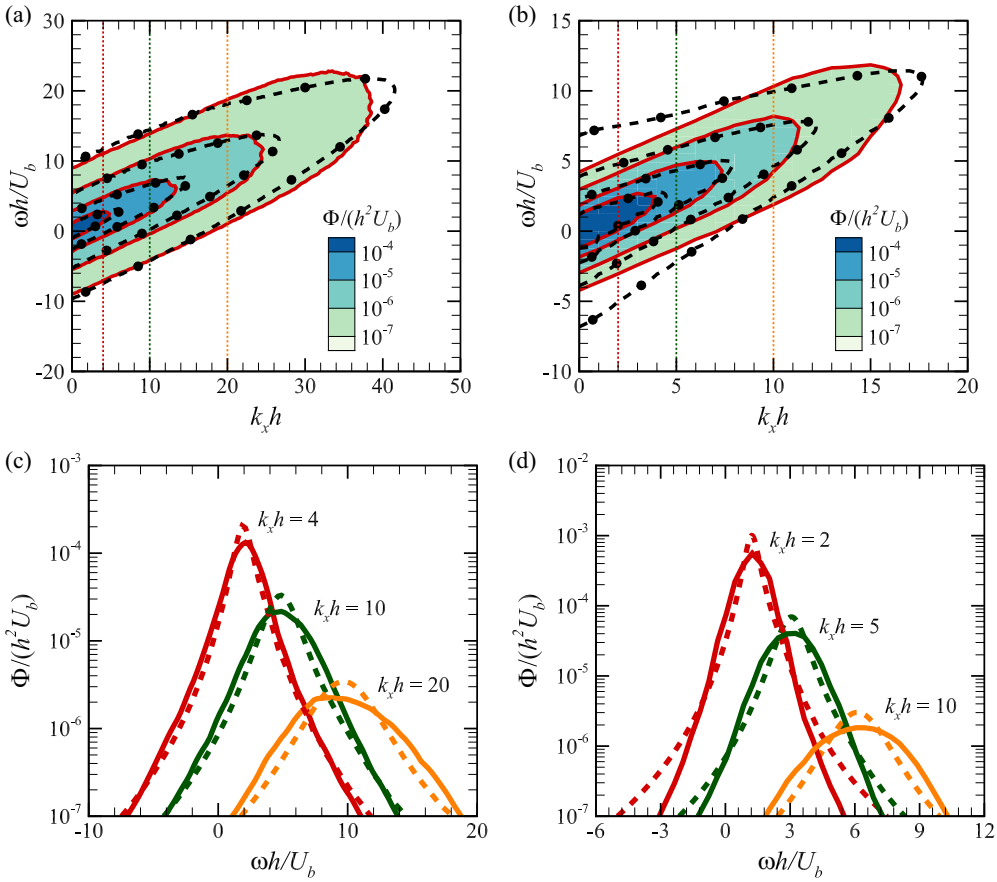

FIG. 9. Comparison of the space-time energy spectra obtained from the DNS and the DAR model with LSE for the streamwise velocity fluctuations at $y_W^+ = 5$ in turbulent channel flows. (a) $\mathrm{Re}_\tau = 550$. Contours obtained from the DNS (colored shades with solid lines) and the combination model (dashed lines with dots). (b) $\mathrm{Re}_\tau = 180$. Contours obtained from the DNS (colored shades with solid lines) and the combination model (dashed lines with dots). (c) $\mathrm{Re}_\tau = 550$. Cuts through space-time energy spectra at three different wave numbers obtained from the DNS (colored solid lines) and the combination model (dashed lines). (d) $\mathrm{Re}_\tau = 180$. Cuts through space-time energy spectra at three different wave numbers obtained from the DNS (colored solid lines) and the combination model (dashed lines).

model with LSE and the DNS are in good agreement. This implies that the present model reproduces the convection velocities of the DNS results. However, the patches of the same contour shades in Figs. 7(a) and 7(d) have different locations since the phases of the velocity fluctuations from the present model are not exactly the same as those from the DNS.

Figure 8 shows the scatter diagrams of the spatial and temporal derivatives of the streamwise velocity components obtained from the DNS and the DAR model with LSE. The scattered point clouds from the present model have the same preference direction, which again confirms that the model reproduces the convection velocities in the DNS. Moreover, although there are no sufficiently scattered points at the edge of the cloud given by the present model, its shape is similar to that of the DNS results. This observation indicates that the space-time distribution of the streamwise velocity components generated by the present model is a good approximation to the DNS results.

Figures 9(a) and 9(b) compare the contours of the space-time energy spectra from the DAR model with LSE and the DNS at $\mathrm{Re}_\tau = 550$ and $\mathrm{Re}_\tau = 180$, respectively. The results from the present

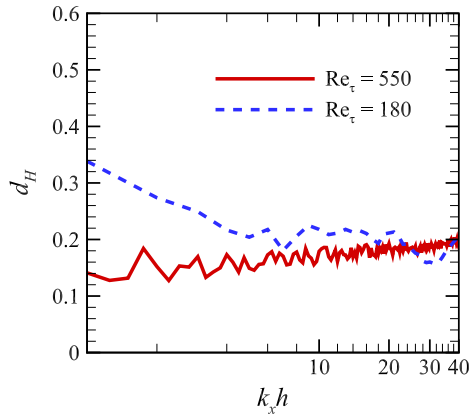

FIG. 10. The Hellinger distance between the model and the DNS results at $\mathrm{Re}_\tau = 550$ and $\mathrm{Re}_\tau = 180$.

model are in agreement with those from the DNS. Figures 9(c) and 9(d) compare the temporal spectra for three different wave numbers from the DNS and the present model. The curves at $\mathrm{Re}_\tau = 550$ are in better agreement than those at $\mathrm{Re}_\tau = 180$. This indicates that the present model becomes better at larger Reynolds numbers.

The differences of the space-time energy spectra between the model and the DNS can be quantified using the Hellinger distance [36], defined as

$$d_H(k_x) = \left[\int \left(\sqrt{\frac{\Phi^{\mathrm{model}}(k_x, \omega)}{\Phi^{\mathrm{model}}(k_x)}} - \sqrt{\frac{\Phi^{\mathrm{DNS}}(k_x, \omega)}{\Phi^{\mathrm{DNS}}(k_x)}} \right)^2 d\omega \right]^{1/2}. \tag{73}$$

The Hellinger distance $d_H = 0$ if and only if $\Phi^{\mathrm{model}} = \Phi^{\mathrm{DNS}}$ and reaches a maximum of $\sqrt{2}$ if Φ^{model} and Φ^{DNS} are significantly different. Figure 10 plots the Hellinger distance between the model and the DNS results at $\mathrm{Re}_\tau = 550$ and $\mathrm{Re}_\tau = 180$. As shown, the values of the Hellinger distance are small compared with the maximum $\sqrt{2}$, indicating the performance of the DAR model with LSE. Furthermore, the Hellinger distance at $\mathrm{Re}_\tau = 550$ is smaller than that at $\mathrm{Re}_\tau = 180$, which implies a better performance of the model at larger Reynolds numbers.

Figure 11 compares the wave-number-dependent convection velocities and spectral bandwidths at $y_W^+ = 5$ obtained from the DNS at $\mathrm{Re}_\tau = 550$ with the results from the DAR model with LSE. We also plot the DNS results at $y_O^+ = 92$, which is used for LSE. Both the convection velocities and spectral bandwidths from the present model are in agreement with those of the DNS. Figure 12 plots similar results at $\mathrm{Re}_\tau = 180$ as Fig. 11. Again, the wave-number-dependent convection velocities and spectral bandwidths from the present model are in agreement with the results from the DNS. Therefore, although there are some differences in the low-level contours of the energy spectra and the tails of the frequency spectra between the present model and the DNS, as shown in Figs. 9(b) and 9(d), the present model can reproduce the first- and second-order moments of the space-time energy spectra of the streamwise velocities conditional at given wave numbers.

Figure 13 plots the line and shade contours of the space-time correlations and the spatial correlations for fixed delay times. The results at $\mathrm{Re}_\tau = 550$ are shown in Figs. 13(a) and 13(c), while the results at $\mathrm{Re}_\tau = 180$ are shown in Figs. 13(b) and 13(d). The contours of the space-time correlation obtained from the model exhibit ellipses, which is consistent with the EA model [38,39]. Although there are some differences in the isocorrelation lines at small levels, the isocorrelation lines at large levels obtained from the model are similar to the DNS results.

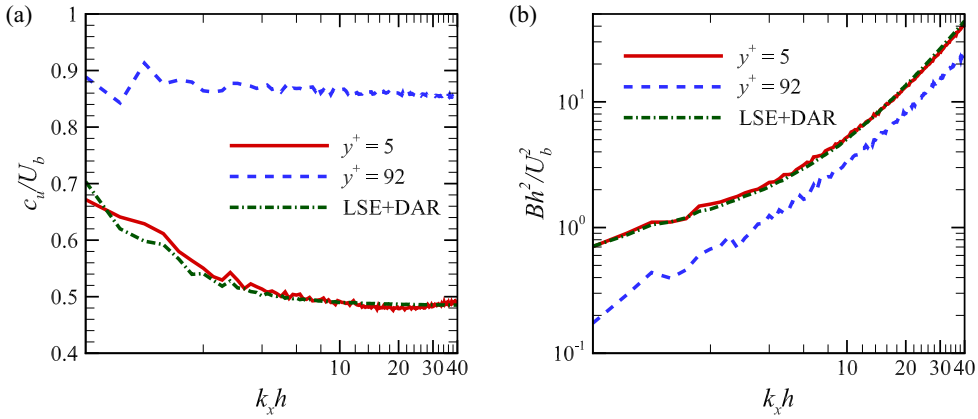

FIG. 11. (a) Wave-number-dependent convection velocities and (b) spectral bandwidths for the streamwise velocity fluctuations in turbulent channel flows at $\mathrm{Re}_\tau = 550$. The results from the DNS at $y_W^+ = 5$ are denoted by red solid lines, the results from the DNS at $y_O^+ = 92$ are denoted by blue dashed lines, and the results from the DAR model with LSE at $y_W^+ = 5$ are denoted by green dash-dotted lines.

VI. CONCLUSION

We developed a dynamic stochastic model for space-time energy spectra in turbulent shear flows. This model incorporates a DAR force into Taylor's model, where this force includes the random sweeping effect and thus depends on the past states. It is shown that the incorporation of a white-in-time random force into Taylor's model results in a divergent spectral bandwidth, while Taylor's model alone incorrectly predicts the vanishing spectral bandwidths. However, the present DAR model reproduces the desired convection velocities and spectral bandwidths. In particular, it predicts the correct scaling exponents of the temporal energy spectra.

We compare the space-time energy spectra obtained from the WW wall model and the LSE approach with the DNS results of turbulent channel flows. The WW wall model notably overestimates the convection velocities and significantly underestimates the spectral bandwidths. The

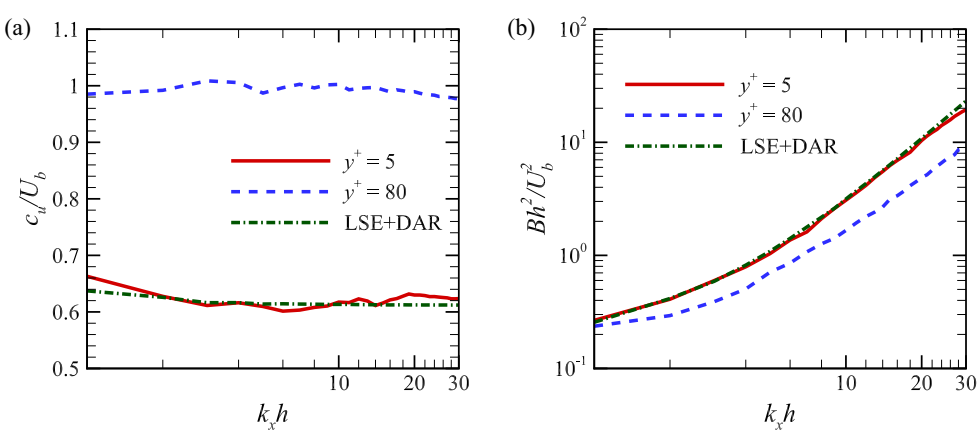

FIG. 12. (a) Wave-number-dependent convection velocities and (b) spectral bandwidths for the streamwise velocity fluctuations in turbulent channel flows at $\mathrm{Re}_\tau = 180$. The results from the DNS at $y_W^+ = 5$ are denoted by red solid lines, the results from the DNS at $y_O^+ = 80$ are denoted by blue dashed lines and the results from the DAR model with LSE at $y_W^+ = 5$ are denoted by green dash-dotted lines.

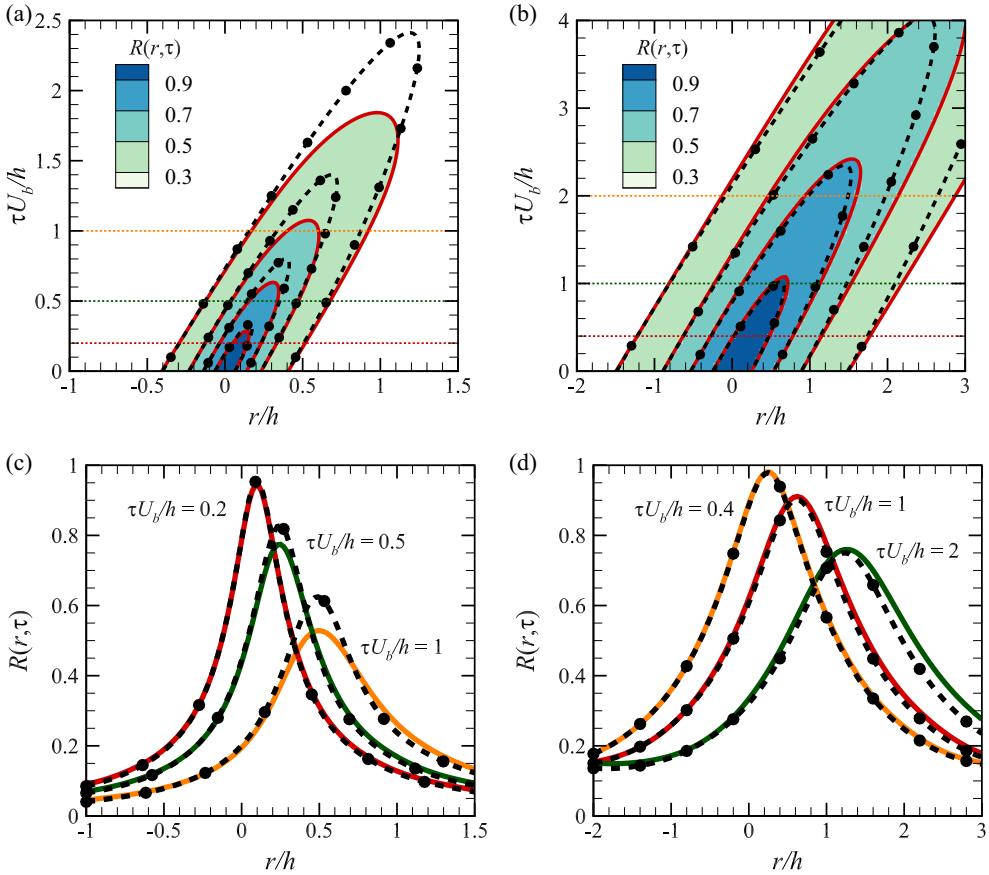

FIG. 13. Comparison of the space-time correlations obtained from the DNS and the DAR model with LSE for streamwise velocity fluctuations at $y_W^+ = 5$ in turbulent channel flows. (a) $\mathrm{Re}_\tau = 550$. Contours obtained from the DNS (colored shades with solid lines) and the DAR model with LSE (dashed lines with dots). (b) $\mathrm{Re}_\tau = 180$. Contours obtained from the DNS (colored shades with solid lines) and the DAR model with LSE (dashed lines with dots). (c) $\mathrm{Re}_\tau = 550$. Cuts through space-time correlations at three different temporal separations obtained from the DNS (colored solid lines) and the DAR model with LSE (dashed lines with dots). (d) $\mathrm{Re}_\tau = 180$. Cuts through space-time correlations at three different temporal separations obtained from the DNS (colored solid lines) and the DAR model with LSE (dashed lines with dots).

LSE approach also incorrectly estimates the convection velocities and spectral bandwidths. The predictions of the WW wall model and the LSE approach on the spectral bandwidths are erroneous because they do not contain sufficient turbulent fluctuations. However, the LSE approach can provide large-scale motions in the near-wall region and thus serve as a suitable input of the DAR model.

The DAR model in combination with LSE can correctly reproduce the space-time energy spectra in the near-wall region, while the DAR model alone can correctly reproduce the space-time energy spectra of velocity fluctuations in the logarithmic region. This provides the possibility of incorporating the DAR model into wall-modeled large-eddy simulations. It is numerically shown that the contours of space-time energy spectra obtained from the DAR model are in agreement with the DNS results. Moreover, the DAR model can reproduce the convection velocities and spectral bandwidths in the DNS. In addition, we explain how to determine the parameters in the DAR model. We note that DAR is a data-refined physical model that consists of Taylor's model with dynamic autoregressive external forcing. It can reproduce the space-time energy spectra in the sense that

the first- and second-order conditional moments are in good agreement with the DNS results. It is expected that the DAR model can be used as an alternative to white-in-time random forcing in turbulence modeling.

The statistical decorrelation of velocity fluctuations in turbulent shear flows is dominated by the convection of small scales by large-scale velocities and small-scale interactions. The convection of small scales by large scales is typically represented by Taylor's hypothesis. The small-scale interaction exhibits two effects: the energy transfers between different scales and the distortion of small eddies by themselves. The energy transfer is conventionally represented by eddy viscosity. The distortion of small eddies is represented by random sweeping. The DAR model represents the three effects by using Taylor's model and DAR forcing so that it can reproduce the space-time energy spectra. In the present study, Taylor's model is used as a prototype. This model can be replaced by other models, such as the resolvent operator and linearized Navier-Stokes equations, to study the space-time dynamics of coherent structures.

ACKNOWLEDGMENTS

This work is supported by NSFC Basic Science Center Program for "Multiscale Problems in Nonlinear Mechanics" (Grant No. 11988102) and National Natural Science Foundation of China (Grants No. 12002344, No. 11232011, and No. 11572331). The authors would like to acknowledge the support from China Postdoctoral Science Foundation (Grant No. 2020M670478), the Strategic Priority Research Program (Grant No. XDB22040104) and the Key Research Program of Frontier Sciences of the Chinese Academy of Sciences (Grant No. QYZDJ-SSW-SYS002).

[1] G. W. He, G. D. Jin, and Y. Yang, Space-time correlations and dynamic coupling in turbulent flows, Annu. Rev. Fluid Mech. **49**, 51 (2017).

[2] R. J. Adrian and P. Moin, Stochastic estimation of organized turbulent structure: homogeneous shear flow, J. Fluid Mech. **190**, 531 (1988).

[3] K. Taira, S. L. Brunton, S. T. M. Dawson, C. W. Rowley, T. Colonius, B. J. McKeon, O. T. Schmidt, S. Gordeyev, V. Theofilis, and L. S. Ukeiley, Modal analysis of fluid flows: An overview, AIAA J. **55**, 4013 (2017).

[4] J. LeHew, M. Guala, and B. J. McKeon, A study of the three-dimensional spectral energy distribution in a zero pressure gradient turbulent boundary layer, Exp. Fluids **51**, 997 (2011).

[5] R. de Kat and B. Ganapathisubramani, Frequency-wavenumber mapping in turbulent shear flows, J. Fluid Mech. **783**, 166 (2015).

[6] G. W. He, M. Wang, and S. K. Lele, On the computation of space-time correlations by large-eddy simulation, Phys. Fluids **16**, 3859 (2004).

[7] M. Wilczek, R. J. A. M. Stevens, and C. Meneveau, Spatio-temporal spectra in the logarithmic layer of wall turbulence: large-eddy simulations and simple models, J. Fluid Mech. **769**, R1 (2015).

[8] G. I. Taylor, The spectrum of turbulence, Proc. R. Soc. London A **164**, 476 (1938).

[9] R. H. Kraichnan, Isotropic turbulence and inertial range structure, Phys. Fluids **9**, 1728 (1966).

[10] J. Jiménez, Cascades in wall-bounded turbulence, Annu. Rev. Fluid Mech. **44**, 27 (2012).

[11] G. Comte-Bellot and S. Corrsin, Simple Eulerian time correlation of full- and narrow-band velocity signals in grid-generated, 'isotropic' turbulence, J. Fluid Mech. **48**, 273 (1971).

[12] R. H. Kraichnan, Kolmogorov's hypotheses and Eulerian turbulence theory, Phys. Fluids **7**, 1723 (1964).

[13] H. Tennekes, Eulerian and Lagrangian time microscales in isotropic turbulence, J. Fluid Mech. **67**, 561 (1975).

[14] M. Wilczek, R. J. A. M. Stevens, and C. Meneveau, Height-dependence of spatio-temporal spectra of wall-bounded turbulence–LES results and model predictions, J. Turbul. **16**, 937 (2015).

[15] B. F. Farrell and P. J. Ioannou, Stochastic forcing of the linearized navier-stokes equations, Phys. Fluids A **5**, 2600 (1993).

[16] B. Bamieh and M. Dahleh, Energy amplification in channel flows with stochastic excitation, Phys. Fluids **13**, 3258 (2001).
[17] M. R. Jovanović and B. Bamieh, Componentwise energy amplification in channel flows, J. Fluid Mech. **534**, 145 (2005).
[18] Y. Hwang and C. Cossu, Amplification of coherent streaks in the turbulent Couette flow: an input-output analysis at low Reynolds number, J. Fluid Mech. **643**, 333 (2010).
[19] Y. Hwang and C. Cossu, Linear non-normal energy amplification of harmonic and stochastic forcing in the turbulent channel flow, J. Fluid Mech. **664**, 51 (2010).
[20] R. Moarref and M. R. Jovanović, Model-based design of transverse wall oscillations for turbulent drag reduction, J. Fluid Mech. **707**, 205 (2012).
[21] L. N. Trefethen, A. E. Trefethen, S. C. Reddy, and T. A. Driscoll, Hydrodynamic stability without eigenvalues, Science **261**, 578 (1993).
[22] B. J. McKeon and A. S. Sharma, A critical-layer framework for turbulent pipe flow, J. Fluid Mech. **658**, 336 (2010).
[23] B. J. McKeon, The engine behind (wall) turbulence: perspectives on scale interactions, J. Fluid Mech. **817**, P1 (2017).
[24] B. F. Farrell and P. J. Ioannou, Perturbation structure and spectra in turbulent channel flow, Theor. Comput. Fluid Dyn. **11**, 237 (1998).
[25] A. Zare, M. R. Jovanović, and T. T. Georgiou, Colour of turbulence, J. Fluid Mech. **812**, 636 (2017).
[26] P. Morra, O. Semeraro, D. S. Henningson, and C. Cossu, On the relevance of Reynolds stresses in resolvent analyses of turbulent wall-bounded flows, J. Fluid Mech. **867**, 969 (2019).
[27] A. Towne, A. Lozano-Durán, and X. Yang, Resolvent-based estimation of space time flow statistics, J. Fluid Mech. **883**, A17 (2020).
[28] B. W. Yang, G. D. Jin, T. Wu, Z. X. Yang, and G. W. He, Numerical implementation and evaluation of resolvent-based estimation for space-time energy spectra in turbulent channel flows, Acta Mech. Sin. **36**, 775 (2020).
[29] M. R. Jovanović, From bypass transition to flow control and data-driven turbulence modeling: an input-output viewpoint, Annu. Rev. Fluid Mech. **53**, 311 (2021).
[30] T. Wu, C. H. Geng, Y. C. Yao, C. X. Xu, and G. W. He, Characteristics of space-time energy spectra in turbulent channel flows, Phys. Rev. Fluids **2**, 084609 (2017).
[31] P. A. Durbin and B. A. P. Reif, *Statistical Theory and Modeling for Turbulent Flows* (John Wiley and Sons, New York, 2011).
[32] A. Zare, T. T. Georgiou, and M. R. Jovanović, Stochastic dynamical modeling of turbulent flows, Annu. Rev. Control Robot. Auton. Syst. **3**, 195 (2020).
[33] J. C. Del Álamo and J. Jiménez, Estimation of turbulent convection velocities and corrections to Taylor's approximation, J. Fluid Mech. **640**, 5 (2009).
[34] H. Werner and H. Wengle, Large-eddy simulation of turbulent flow over and around a cube in a plate channel, in *Turbulent Shear Flows 8* (Springer, New York, 1993), pp. 155–168.
[35] W. J. Baars, N. Hutchins, and I. Marusic, Spectral stochastic estimation of high-Reynolds-number wall-bounded turbulence for a refined inner-outer interaction model, Phys. Rev. Fluids **1**, 054406 (2016).
[36] T. Wu and G. W. He, Local modulated wave model for the reconstruction of space-time energy spectra in turbulent flows, J. Fluid Mech. **886**, A11 (2020).
[37] M. Wilczek and Y. Narita, Wave-number-frequency spectrum for turbulence from a random sweeping hypothesis with mean flow, Phys. Rev. E **86**, 066308 (2012).
[38] G. W. He and J. B. Zhang, Elliptic model for space-time correlations in turbulent shear flows, Phys. Rev. E **73**, 055303(R) (2006).
[39] X. Zhao and G. W. He, Space-time correlations of fluctuating velocities in turbulent shear flows, Phys. Rev. E **79**, 046316 (2009).
[40] C. H. Geng, G. W. He, Y. S. Wang, C. X. Xu, A. Lozano-Durán, and J. M. Wallace, Taylor's hypothesis in turbulent channel flow considered using a transport equation analysis, Phys. Fluids **27**, 025111 (2015).